

# Storm phase-partitioned rates and budgets of global Alfvénic energy deposition, electron precipitation, and ion outflow



Spencer M. Hatch<sup>a,\*</sup>, James LaBelle<sup>a</sup>, Christopher C. Chaston<sup>b</sup>

<sup>a</sup> Department of Physics and Astronomy, Dartmouth College, Hanover, NH, USA

<sup>b</sup> Space Sciences Laboratory, University of California, Berkeley, CA, USA

## ARTICLE INFO

### Keywords:

Inertial Alfvén waves  
ULF waves  
Geomagnetic storms  
Dynamic coupling  
Ion outflow  
Electron acceleration

## ABSTRACT

We review the role of Alfvén waves in magnetosphere-ionosphere coupling during geomagnetically active periods, and use three years of high-latitude FAST satellite observations of inertial Alfvén waves (IAWs) together with 55 years of tabulated measurements of the *Dst* index to answer the following questions: 1) How do global rates of IAW-related energy deposition, electron precipitation, and ion outflow during storm main phase and storm recovery phase compare with global rates during geomagnetically quiet periods? 2) What fraction of net IAW-related energy deposition, electron precipitation, and ion outflow is associated with storm main phase and storm recovery phase; that is, how are these budgets partitioned by storm phase? We find that during the period between October 1996 and November 1999, rates of IAW-related energy deposition, electron precipitation, and ion outflow during geomagnetically quiet periods are increased by factors of 4–5 during storm phases. We also find that ~62–68% of the net Alfvénic energy deposition, electron precipitation, and ion outflow in the auroral ionosphere occurred during storm main and recovery phases, despite storm phases comprising only 31% of this period. In particular storm main phase, which comprised less than 14% of the three-year period, was associated with roughly a third of the total Alfvénic energy input and ion outflow in the auroral ionosphere. Measures of geomagnetic activity during the IAW study period fall near corresponding 55-year median values, from which we conclude that each storm phase is associated with a fraction of total Alfvénic energy, precipitation, and outflow budgets in the auroral ionosphere that is, in the long term, probably as great or greater than the fraction associated with geomagnetic quiescence for all times except possibly those when geomagnetic activity is protractedly weak, such as solar minimum. These results suggest that the budgets of IAW-related energy deposition, electron precipitation, and ion outflow are roughly equally partitioned by geomagnetic storm phase.

## 1. Introduction

The term “geomagnetic storm” has come to refer to efficient coupling between the solar wind and the magnetosphere (Kamide et al., 1998; Tsurutani et al., 2006b; Guo et al., 2011) over periods between several hours and several days (Gonzalez et al., 1994), where the associated interplanetary conditions include a combination of either gradual or sudden increases solar wind speeds and densities (e.g., Cane and Richardson, 2003; Tsurutani et al., 2006a) or evolution of the interplanetary magnetic field to an orientation that is favorable to reconnection between solar and terrestrial magnetic fields lines (Dunlop et al., 2009), or both (Newell et al., 2007).

Storm periods are functionally defined in the magnetosphere by both electron loss and energization (Hudson et al., 2012; Anderson et al.,

2015; Gao et al., 2015) and wave energization (Brito et al., 2012) in the radiation belts, as well as population of the ring current with energetic particles, of which a large fraction are terrestrial ions (Hamilton et al., 1988; Chaston et al., 2016). At mid-to low-latitude terrestrial observatories geomagnetic storms are manifest as a weakening of the horizontal component of the terrestrial magnetic field, usually quantified by the *Dst* or *SYM-H* index. In terms of auroral precipitation, which is commonly classified as either diffuse, monoenergetic, or broadband via spectral characteristics, broadband aurora are the most responsive to conditions in the solar wind (Newell et al., 2009) and to substorm onset (Newell et al., 2010), during and after which broadband aurora tend to be found at lower latitudes (Lee et al., 2010).

Studies in the past two decades have highlighted the relationship between broadband aurora, which consists of electron energy fluxes over

\* Corresponding author.

E-mail address: [Spencer.M.Hatch.GR@dartmouth.edu](mailto:Spencer.M.Hatch.GR@dartmouth.edu) (S.M. Hatch).

a range of energies that are usually below 1 keV (Newell et al., 2009), and Alfvén waves. Evidence for this relationship is presented by Chaston et al. (2007a), who demonstrate that Alfvénic activity is strongly correlated with auroral activity, while several theoretical studies (e.g., Hasegawa, 1976; Kletzing, 1994; Kletzing and Hu, 2001; Lysak and Song, 2003; Génot et al., 2004; Chen et al., 2005; Tanaka et al., 2005b; Watt et al., 2005; Watt and Rankin, 2012) have shown that Alfvén waves on kinetic scales interact with and accelerate electrons, particularly over the altitude range where the electron inertial length becomes comparable to the Alfvén speed, between  $\sim 1\text{--}2 R_E$  (Chaston et al., 2003a; Watt and Rankin, 2009). Observational studies in support of these mechanisms are likewise many, a small subset of which includes observations in the plasma sheet (Keiling et al., 2000, 2002), the plasma sheet boundary layer (Takada et al., 2006), the mid-altitude cusp and low-latitude boundary layer (Bogdanova et al., 2004), and above the auroral ionosphere (Andersson et al., 2002; Tanaka et al., 2005a; Chaston et al., 2006). (See also reviews of small-scale Alfvén waves (Stasiewicz et al., 2000) and Alfvénic turbulence (Wu et al., 2016) as well as references therein.)

Much of the present picture of coupling and feedback mechanisms between the ionosphere and the magnetosphere has emerged in the past decade (Lysak, 2004; Thayer and Semeter, 2004; Lotko, 2007; Kronberg et al., 2014; Lotko et al., 2014; Lysak et al., 2015; Welling et al., 2015; Khazanov et al., 2016). During geomagnetically disturbed periods, dynamic mechanisms for magnetosphere-ionosphere coupling become important (Song and Vasylinas, 2014; Mishin et al., 2015) and phenomena occurring on short time scales ( $\lesssim 100$  s) cannot be accommodated by paradigms that are based on electrostatic magnetosphere-ionosphere coupling (Lotko, 2004). Periods of dynamic coupling, during which effects associated with an induction electric field or the displacement current (or both) can be pronounced, are associated with Alfvén waves (Knudsen, 1996; Yoshikawa and Itonaga, 1996; Rankin et al., 1999; Lysak and Song, 2000, 2006; Cosgrove, 2016) and with transient/wave phenomena otherwise (Mareschal, 1976; Hoshino et al., 2001; Delcourt, 2002; Liemohn and Kozyra, 2002; Song and Lysak, 2006; Ohtani et al., 2010).

In their examination of the effect of geomagnetic storms on inertial Alfvén wave (IAW) activity, Hatch et al. (2016) have shown that the occurrence rate of IAWs, as well as the associated energy deposition, precipitation, and ion outflow, respond rapidly and dramatically to storm sudden commencement. In view of the relative importance of dynamic/inductive coupling during geomagnetically disturbed periods, the natural questions arising from but not addressed by their study are the following: 1) How much do geomagnetic storms alter the global rates of Alfvénic energy input, electron precipitation, and ion outflow that are typical of geomagnetically quiescent periods? 2) What is the relative contribution of each storm phase to the long-term budgets of Alfvénic energy deposition, precipitation, and outflow in the auroral ionosphere? The purpose of this study is to address these questions.

Because this study builds upon work performed by Hatch et al. (2016), in Section 2 we summarize the methodology and key findings of their study. In Section 3 we present storm phase-partitioned rates of energy deposition, electron precipitation, and ion outflow associated with IAWs in the Northern and Southern Hemisphere. Based on the frequency of each storm phase during the three-year study period, in Section 4 we calculate storm phase-partitioned budgets of IAW-related energy deposition, precipitation, and outflow, and compare various measures of geomagnetic activity during the study period with corresponding measures during a 55-year period covering  $\sim 5$  solar cycles. We then summarize and conclude.

## 2. Review of stormtime Alfvénic activity in the auroral zone

Hatch et al. (2016) use a database of IAW observations made by the FAST satellite in the magnetosphere-ionosphere transition region from October 1996 to November 1999, together with *Dst* measurements and the NOAA Geomagnetic Sudden Storm Commencements data set.

To identify IAWs Hatch et al. (2016) locate periods during which the field-aligned current  $|J_{\parallel}| \geq 10 \mu\text{A}/\text{m}^2$ , where  $J_{\parallel}$  is estimated via the slope in the axial (approximately east-west) component of FAST fluxgate magnetometer data using Ampère's law. Accurate identification is ensured by requiring corresponding observations to meet several additional criteria dealing with, for example, minimum fluctuation in  $B$  relative to the background magnetic field  $B_0$ , minimum fluctuation in the spin-plane electric field  $E$ , instrument modes with sample rates appropriate for IAW identification, minimum field-aligned electron fluxes, appropriate frequency restrictions, and application of the so-called E-over-B test (e.g., Aikio et al., 1996; Stasiewicz et al., 1998; Keiling, 2009).

As applied in this study and in the work of Hatch et al. (2016), the E-over-B test requires that the change in the spin-plane electric field  $\Delta E_{\text{sp}}$  and the change in the axial component of the magnetic field  $\Delta B_{\text{axial}}$  meet the condition  $0.1 \leq |\Delta E_{\text{sp}}/\Delta B_{\text{axial}}|/v_A \leq 10$ . Chaston et al. (2007a) use a nearly identical form of this test for IAW identification.

After identifying all qualifying IAW observations during the three-year period, Hatch et al. (2016) associate each IAW with geomagnetic storm phases using two approaches for storm identification. The first approach follows the methodology of Chaston et al. (2015), who classify all times for which *Dst*  $> -20$  nT as “non-storm” periods, and classifies all times for which *Dst*  $\leq -20$  nT as storm periods. Storm phase is then identified by smoothing *Dst* over a 6-h window and examining the slope of the smoothed *Dst* time series; “main phase” is defined as periods when  $\frac{dD_{\text{st}}}{dt} \leq 0$ , and “recovery phase” as periods when  $\frac{dD_{\text{st}}}{dt} > 0$ . The second approach begins with the methodology of Anderson et al. (2015), who define a large geomagnetic storm as any instance of  $D_{\text{st}_{\text{min}}} \leq -50$  nT that is global for 16 h on either side of  $D_{\text{st}_{\text{min}}}$ , and that corresponds to a drop in *Dst* of at least 55 nT within 16 h preceding  $D_{\text{st}_{\text{min}}}$ . Large storms thus identified are then aligned with entries in the NOAA Geomagnetic Storm Sudden Commencements data set (<https://catalog.data.gov/dataset/geomagnetic-storm-sudden-commencements>), resulting in selection of 31 large storms for the three-year IAW study period.

Associating IAW observations with each storm phase identified by the first method above, Hatch et al. (2016) show that storm main phase corresponds to order-of-magnitude enhancements in IAW-related Poynting fluxes and precipitating electron energy fluxes, with strong enhancements in electron energy fluxes below  $70^\circ$  invariant latitude (ILAT) over a broad range of local times on the nightside, and in the premidnight sector these enhanced Poynting and electron energy fluxes persist into the recovery phase. They also find that during storm main phase IAW-related upward ion fluxes primarily below  $70^\circ$  ILAT increase by up to two orders of magnitude at various local times on both dayside and nightside, with the enhancements being most pronounced and widespread on the dayside. During “non-storm” times the locations of most frequent IAW activity are centered at roughly noon magnetic local time (MLT) and above  $70^\circ$  ILAT on the dayside, and premidnight at slightly lower latitudes on the nightside; during storm main phase, however, the primary sites of IAW activity on the dayside are found below  $70^\circ$  ILAT and postnoon, extending into the dusk sector, and on the nightside extending over a wide range of local times primarily below  $70^\circ$  ILAT.

To explicitly demonstrate that the foregoing effects are a consequence of geomagnetic storms, Hatch et al. (2016) perform a superposed epoch analysis of IAW activity relative to storm sudden commencement using storm onsets identified by the second method above. Fig. 1 (Fig. 4a in Hatch et al. (2016)) shows that the probability of IAW observation promptly increases at storm commencement on both dayside and nightside, and within 2 h (i.e., the histogram resolution) reaches a maximum that is several times background values of Alfvén activity. Similar enhancements in IAW-related loss-cone electron energy flux, upward ion flux, and Alfvénic Poynting flux also appear (Fig. 4b–d in Hatch et al., 2016), then taper to background levels  $\sim 20$  h after storm commencement.

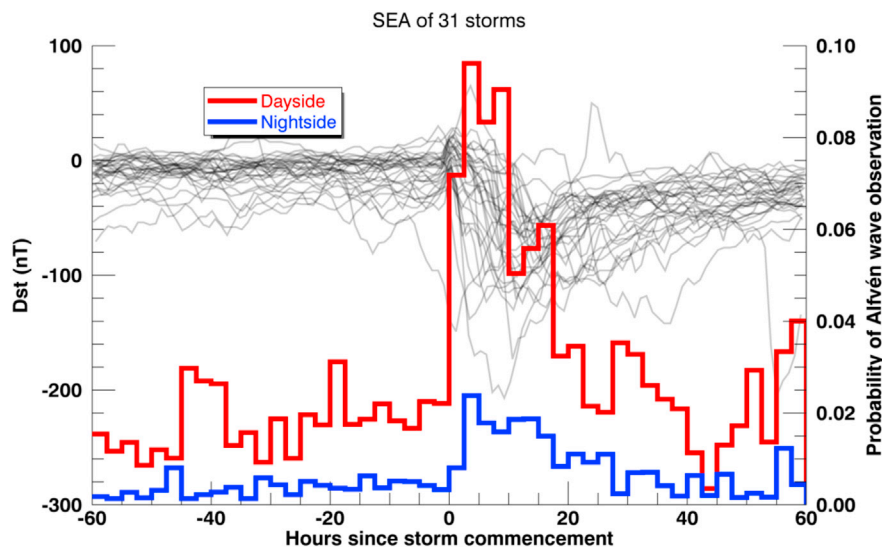


Fig. 1. Response of inertial Alfvén wave occurrence rates to storm sudden commencement on dayside (red) and nightside (blue), for 120 h around storm sudden commencement ( $t = 0$ ). Dst time series for each of 31 storms occurring between October 1996 and November 1999 are shown as transparent black traces in the background [Originally Fig. 4a in Hatch et al. (2016); reproduced with permission of John Wiley & Sons, Inc.]. (For interpretation of the references to colour in this figure legend, the reader is referred to the web version of this article.)

### 3. IAW database and time-averaged fluxes

The IAW database we use here is similar to that described by Hatch et al. (2016), the only differences being that in this study we use  $1 \mu\text{A}/\text{m}^2$  as the threshold for minimum field-aligned current density instead of  $10 \mu\text{A}/\text{m}^2$ , we exclude observations made below 750 km in order to avoid ionospheric Alfvén resonator effects (Poliakov and Rapoport, 1981; Lysak, 1993; Grzesiak, 2000; Chaston et al., 2002; Hirano et al., 2005; Rother et al., 2007) that might otherwise lead to overestimation of the measures of Alfvénic activity presented in this study, and all fluxes are mapped to 100 km using AACGM\_v2 coordinates (Shepherd, 2014).

We have reduced the minimum field-aligned current density threshold in this study because the  $10\text{-}\mu\text{A}/\text{m}^2$  current density threshold applied by Hatch et al. (2016) appears to be biased against nightside IAW observations relative to those on the dayside: 24.8% of nightside IAW observations correspond to current densities that fall below  $10 \mu\text{A}/\text{m}^2$ , while only 8.7% of dayside IAW observations fall below this threshold.

The physical source of this bias may be the steeper gradients in and overall lower values of nightside electron density relative to those on the dayside [Fig. 1 in Kelley (1989); Cattell et al., 2006], which cause the energy carried by IAWs to be more efficiently dissipated and reflected on the nightside (Chaston et al., 2003b, a; Hatch et al., 2016). We have therefore attempted to remove the bias against nightside IAW observations by lowering this threshold to  $1 \mu\text{A}/\text{m}^2$ . Interested readers may consult Appendix A, which contains a condensed version of the analysis we present in the next section using the original current density threshold imposed by Hatch et al. (2016). The updated database contains 334,915 and 121,719 IAW observations in the Northern and Southern Hemisphere, respectively.

We begin with the same set of flux quantities used by Hatch et al. (2016); these are Poynting flux, electron energy flux, and upward ion flux, where the latter two fluxes are integrated along the spacecraft trajectory over the duration of the IAW observation and then spatially averaged.

To obtain loss-cone electron number and energy fluxes, electron electrostatic analyzer (ESA) measurements are integrated over all energies above the spacecraft potential up to the detector limit at 30 keV (Carlson et al., 2001), and over the range of pitch angles within the earthward portion of the loss cone calculated via International Geomagnetic Reference Field 11 (IGRF 11).

To obtain upward ion number and energy fluxes, ion ESA

measurements are integrated over all energies above the spacecraft potential up to 500 eV in order to avoid the contribution from plasma sheet ions, and over the  $90^\circ$  range of pitch angles that is both anti-earthward and leeward the motion of the spacecraft; the latter requirement serves to exclude ram ions. The resulting ion number and energy fluxes are then doubled to account for neglecting the range of pitch angles that correspond to ram ions.

For the set of flux measurements  $\{q_i; i = 1 \dots N\}$  within each MLT-ILAT bin Hatch et al. (2016) calculate and report the statistic

$$\bar{Q} = \exp \left[ \left( \frac{\sum_i^N \ln q_i}{N} \right) \right]. \quad (1)$$

The distributions of IAW-associated Poynting flux, upward ion flux, and electron energy flux measurements in each MLT-ILAT bin are all approximately log normal (Fig. 3 in Hatch et al., 2016); the sample log average  $\bar{Q}$  is therefore the appropriate estimator of the population median for each set of flux measurements.

In this study we wish to calculate average temporal rates of Alfvénic energy deposition, precipitation, and outflow in each hemisphere. That the statistic  $\bar{Q}$  is inappropriate for this objective may be seen by briefly considering a hypothetical situation: Suppose FAST only rarely observes IAWs within an MLT-ILAT bin (say, less than 5% of the time that FAST spends in that bin), but during period of unusual geomagnetic activity the satellite observes a number of IAW current filaments associated with intense upward ion fluxes while traversing the bin. Because  $\bar{Q}$  takes no account of the low rate of IAW observation associated with that bin,  $\bar{Q}$  is prone to overestimation of the actual temporally averaged upward ion flux associated with IAWs.

In order to account for both the intensity and the duration of the flux quantities associated with each IAW observation, as well as the overall frequency of IAW observations within each MLT-ILAT bin, for each flux quantity we instead calculate the time-averaged flux

$$\langle Q \rangle = \left( \frac{\sum_i^N q_i \tau_i}{T_{128}} \right), \quad (2)$$

where  $N$  is the number of IAW observations,  $\tau_i$  is the temporal width of the  $i$ th IAW observation,  $q_i$  is an individual flux measurement, and  $T_{128}$  is the total amount of time that FAST was within that MLT-ILAT bin while

the survey-mode sampling rate of the fluxgate magnetometer  $f_{FG}$  was appropriate for IAW identification ( $f_{FG} \geq 128$  S/s).

How  $\langle Q \rangle$  accounts for the frequency of IAW observation is illustrated by setting  $q_i = 1$  in (2), which yields the quantity  $\sum_i^N \tau_i / T_{128}$  that Hatch et al. (2016) term the “IAW probability of observation” (shown as Fig. 2a

in their study). The reliance of  $\langle Q \rangle$  on IAW observation frequency means that for a given set of flux measurements the time-averaged flux estimate  $\langle Q \rangle$  (hereafter “average flux”) is usually less than the corresponding estimate  $\bar{Q}$ . We make a more detailed comparison between these two types of averages in the following section.

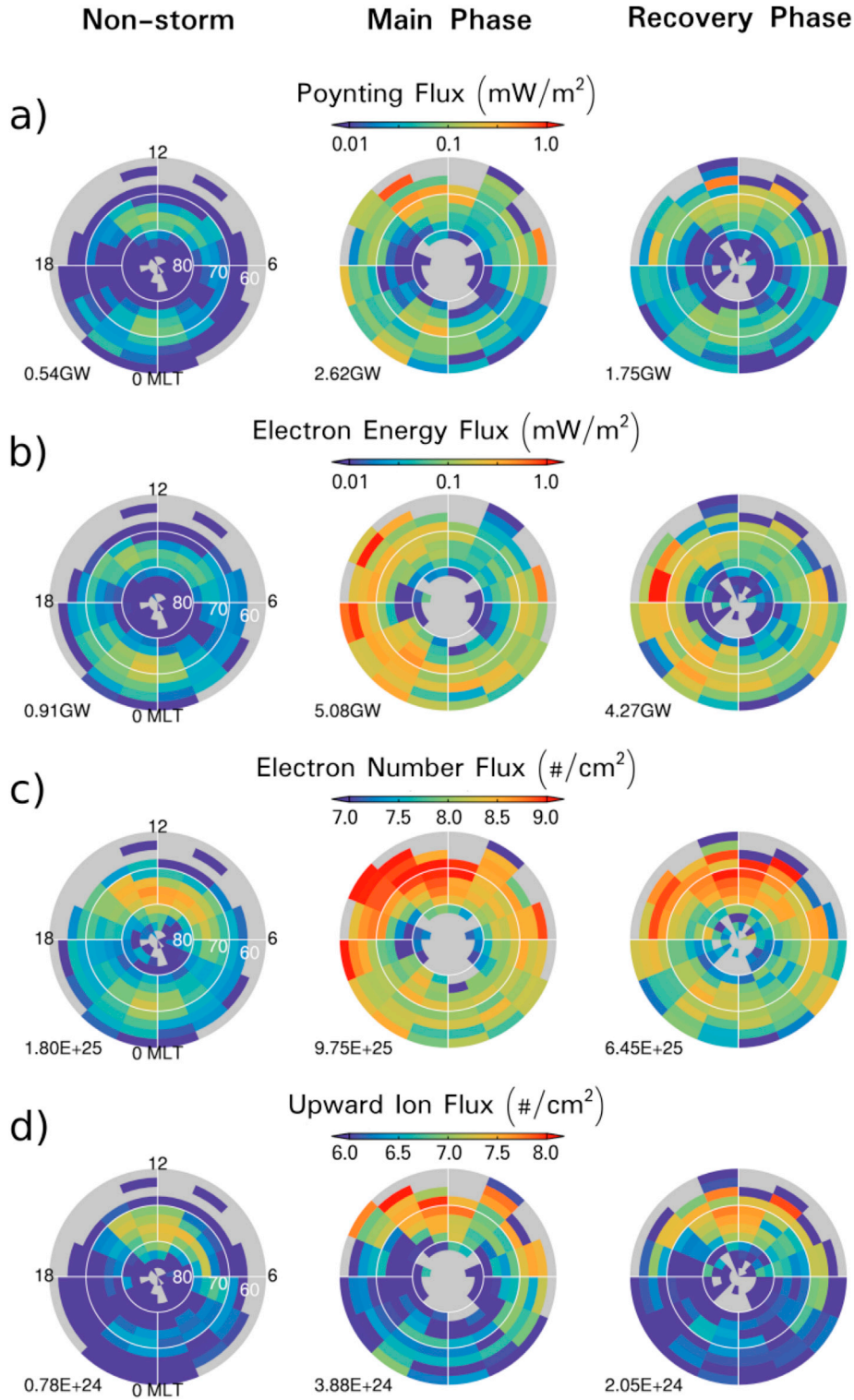


**Fig. 2.** Average fluxes associated with small-scale Alfvén waves in the Northern Hemisphere during geomagnetically quiescent periods (left panels), storm main phase (center panels), and storm recovery phase. The size of each bin is 1.5 MLT  $\times$  2.5° ILAT, and each bin containing fewer than 8 IAW observations is shown in gray. The integrated hemispheric rate of either energy deposition (GW), precipitation ( $10^{25}$ /s), or outflow ( $10^{24}$ /s) is shown at bottom left in each panel. (a) Poynting flux. (b) Loss-cone electron energy flux. (c) Loss-cone electron number flux. (d) Upward ion flux.

#### 4. Rates of IAW-related energy deposition, electron precipitation, and ion outflow

The average flux ( $Q$ ) for each flux quantity in the Northern Hemisphere is shown in Fig. 2, which displays the average Poynting flux (Fig. 2a), loss-cone electron energy flux (Fig. 2b), loss-cone electron number flux (Fig. 2c), and ion outflow (Fig. 2d) observed in coincidence with IAWs. Each figure displays statistics for geomagnetically quiescent periods during which  $Dst > -20$  nT (left panels), storm main phase (center panels), and storm recovery phase (right panels). For each phase the integrated hemispheric rate of either energy deposition, precipitation, or ion outflow is shown at bottom left in the corresponding panel.

Each hemispheric rate is obtained by first multiplying the average flux ( $Q$ ) within each MLT-ILAT bin by the corresponding bin area at 100 km, resulting in a local rate for each MLT-ILAT bin. Local rates are then summed to give a hemispheric rate. In calculating hemispheric rates we impose  $N_{\min} = 8$  as the minimum number of IAW observations within each MLT-ILAT bin in order to be displayed. Each bin associated with  $N < N_{\min}$  IAW observations is shown in gray in Fig. 2, and does not contribute to the calculated hemispheric rate.

We have selected  $N_{\min}$  by first calculating the coefficient of variation

$$\nu = \frac{\sigma}{\mu} \quad (3)$$

for the set of time-weighted flux measurements  $q_i\tau_i$  within each MLT-ILAT bin, where  $\mu = (\sum_i^N q_i\tau_i)/N$  is the sample mean of the distribution of time-weighted flux measurements, and  $\sigma^2 = \sum_i^N (q_i\tau_i - \mu)^2/(N-1)$  is the sample variance. For each set of measurements  $\{q_i\tau_i, i = 1 \dots N\}$ ,  $\nu$  lies between 0 and 1 and trends toward smaller values with increasing number of IAW observations  $N$ . For every panel shown in Fig. 2 (i.e., for all flux quantities and storm phases) the selection  $N_{\min} = 8$  is such that  $\nu < 0.33$  for  $\geq 77\%$  of all MLT-ILAT bins with  $N \geq N_{\min}$ .

During geomagnetically quiescent periods (left panels) the prominent sites of IAW-related energy deposition, electron precipitation, and ion outflow are all primarily postnoon and premidnight. The similar morphologies arise from the method for averaging just described, and are generally in correspondence with the features in the “non-storm” distribution of IAW probability of occurrence shown in the left panel of Fig. 2a in Hatch et al. (2016). These enhancements are moreover in roughly the same location as the enhancements in previously published distributions of observed (Keiling et al., 2003; Chaston et al., 2007b) and simulated (Lotko et al., 2014; Zhang et al., 2014) Alfvénic Poynting flux, and bear morphological resemblance to the “low solar wind driving” distribution of broadband electron precipitation observed by DMSP (Fig. 4a in Newell et al. (2009)) except in 9.5–14.5 MLT. In this MLT range the (Newell et al., 2009) algorithm requires a differential energy flux  $dJ_E/dE > 2.0 \times 10^8$  eV/(cm<sup>2</sup> s sr eV) in at least one ESA energy channel at or above 300 eV in order for precipitation to be identified as broadband. (At all other local times the threshold energy is 140 eV)

During storm main phase dayside increases in average Poynting flux, electron number flux, and upward ion flux are greatest over local times extending from 7.5 to 16.5 MLT and from latitudes extending between roughly 65° and 73° ILAT, with the most intense rates located postnoon and extending nearly to 62° ILAT (Fig. 2a, c, and d). Enhanced electron energy flux is observed primarily in the dusk sector (center panel, Fig. 2b). On the nightside, increases likewise pervade almost all local times and extend to the edge of the study region at 60° ILAT. The transition of peak activity to overall lower latitudes relative to quiescent periods agrees with the anticipated expansion of the auroral oval during geomagnetically active periods.

Average fluxes during storm recovery phase are generally intermediate to those observed during quiescence and storm main phase, though some differences are apparent. For example the storm-enhanced rate of electron energy deposition and precipitation in the dusk sector persists into recovery phase (right panels in Fig. 2b and c, respectively), in some

locations even exceeding main phase-enhanced rates. There are also relatively clear low-latitude enhancements after 0 MLT in both electron precipitation and ion outflow (Fig. 2c and d, respectively) during recovery phase.

As described in Section 3 the average fluxes shown in Fig. 2 are overall lower than the corresponding log-averaged fluxes presented by Hatch et al. (2016). For instance the enhancements in Alfvénic Poynting flux shown in the left panel of Fig. 2a peak near 0.1 mW/m<sup>2</sup>, but Poynting fluxes in the left panel of Fig. 2a in Hatch et al. (2016) are almost uniformly of order 1 mW/m<sup>2</sup>. With regard to morphology cusp-region and premidnight features in Fig. 2a contrast, for example, with the quiet-time distribution of Alfvénic Poynting flux shown in the left panel of their Fig. 2b, which is relatively featureless. Other instances of dissimilar features could be identified; all reflect differences in the type of average that each study employs.

Fig. 3 shows Southern Hemisphere average fluxes for the same quantities presented in Fig. 2. For each storm phase these exhibit trends similar to those noted for corresponding quantities in the Northern Hemisphere, except that the integrated hemispheric rates of IAW-related energy deposition, electron precipitation, and ion outflow (shown at bottom left in each panel of Fig. 3a–d) are all greatest during storm recovery phase, opposite the stormtime trends of corresponding rates in the Northern Hemisphere. The difference in the observed rate of hemispheric ion outflow is greatest, increasing by 150% from  $1.54 \times 10^{24}$  s<sup>-1</sup> during main phase to  $3.91 \times 10^{24}$  s<sup>-1</sup> during recovery phase; the observed rate of electron precipitation also notably differs, increasing by 45% from  $5.42 \times 10^{25}$  s<sup>-1</sup> during storm main phase to  $7.87 \times 10^{25}$  s<sup>-1</sup> during storm recovery phase.

As in Fig. 2, each MLT-ILAT bin with  $N < N_{\min} = 8$  in Fig. 3 is shown in gray and does not contribute to the calculated hemispheric rate. For Southern Hemisphere IAW observations, the selection  $N_{\min} = 8$  is such that within every panel shown in Fig. 2,  $\nu \leq 0.33$  for  $\geq 67\%$  of all MLT-ILAT bins with  $N \geq N_{\min}$ .

#### 5. Discussion

Northern Hemisphere rates of each quantity presented in Fig. 2 for each storm phase are shown in Table 1. Global (combined Northern and Southern Hemisphere) rates are also shown in parentheses on the right side of each Northern Hemisphere rate.

Table 1 shows that during storm main phase the rate of each quantity shown in Figs. 2 and 3 is often several times the corresponding rate during quiescent periods. Northern Hemisphere rates of Alfvénic wave and electron energy deposition increase by factors of 4–5, while rates of electron precipitation and outflowing ion rates both increase by a factor of 5 or more. It is evident that the storm-enhanced rates of wave (Figs. 2a and 3a) and electron (Figs. 2b and 3b) energy deposition associated with storm main and recovery phase are due to relatively uniform contributions from each local time sector, whereas the enhanced rates of electron precipitation (Figs. 2c and 3c) and outflowing ions (Figs. 2d and 3d) are largely due to the dramatic increases in corresponding average fluxes on the dayside.

The main phase-enhanced rates of energy deposition and electron precipitation in the Northern Hemisphere diminish slightly during recovery phase, but are still greater than quiescent rates by at least a factor of 3. The rate of ion outflow is less sustained during recovery phase, though still greater than the rate during quiescence by a factor of 2.6. Incidentally, for every phase Fig. 2b–d and 3b–d generally suggest that ion outflow is better correlated with electron number flux than with electron energy flux. Strangeway et al. (2005) report a similar result; using multi-regression analysis they show that ion outflow is significantly and positively correlated with precipitating electron number flux, while the correlation between ion outflow and electron energy flux is insignificant.

Accounting for the net duration of each phase for the three-year

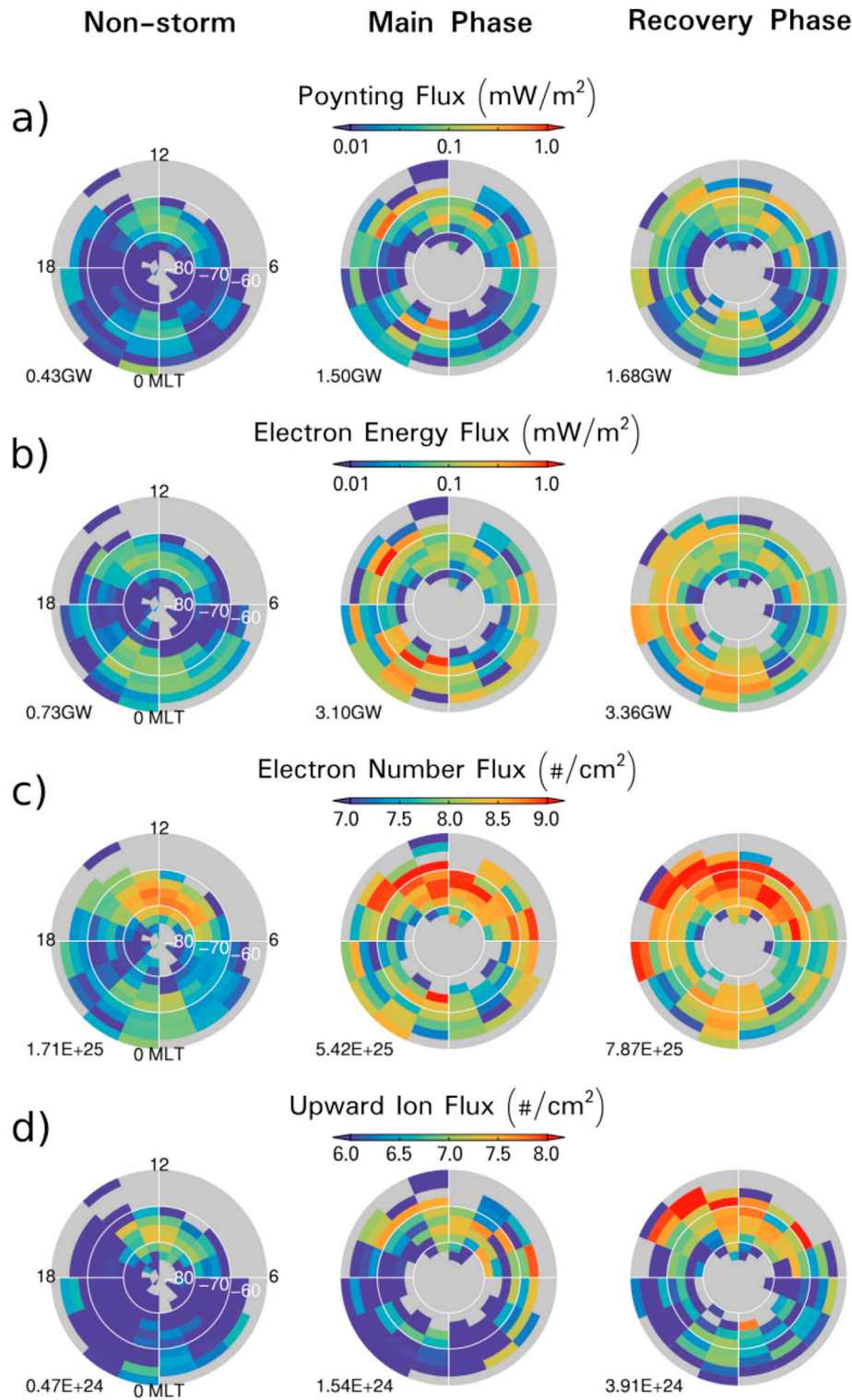


**Fig. 3.** Average fluxes associated with IAWs in the Southern Hemisphere during geomagnetically quietest periods (left panels), storm main phase (center panels), and storm recovery phase (right panels). As in Fig. 2 integrated hemispheric rates are shown at bottom left in each panel, and each 1.5 MLT  $\times$  2.5° ILAT bin containing fewer than 8 IAW observations is shown in gray. Relative to Northern Hemisphere statistics (Fig. 2) the higher number of gray bins in each panel reflects the overall lower number of Southern Hemisphere IAW observations. (a) Poynting flux. (b) Loss-cone electron energy flux. (c) Loss-cone electron number flux. (d) Upward ion flux.

period covered in this study (two uppermost rows, Table 1) the relative contributions of each phase to net Alfvénic energy deposition, electron precipitation, and ion outflow budgets are shown below corresponding rates in Table 1. In the Northern Hemisphere each phase is associated with 30–36% of the total Alfvénic energy deposition and electron precipitation while the range of contributions of each storm phase to ion

outflow is more variable, ranging instead between 25% and 38%.

In light of the net duration of storm main phase, less than 1/6 of the total study period, its association with 33–37% of the total energy, precipitation, and outflow budgets of IAWs in the Northern Hemisphere seems remarkable. Additionally, storm main and recovery phase in combination are associated with between 62% and 69% of the Northern

**Table 1**  
Storm phase-partitioned rates and budgets of Alfvénic energy deposition, precipitation, and ion outflow in the Northern Hemisphere.<sup>a</sup>

	Quiescence	Main Phase	Recovery Phase	M+R Combined
<b>FAST Study Period<sup>b</sup></b>				
Time (days)	310.4	60.4	78.2	138.6
% Total	69.1	13.4	17.4	30.8
<b>IAW Observations</b>				
N	187,871 (252,206)	44,799 (60,177)	60,611 (85,555)	105,410 (145,732)
<b>Wave Energy Deposition</b>				
Rate (GW)	0.54 (0.97)	2.62 (4.12)	1.75 (3.43)	
% Total	36 (37)	34 (30)	30 (33)	64 (63)
<b>Electron Energy Deposition</b>				
Rate (GW)	0.91 (1.64)	5.08 (8.18)	4.27 (7.63)	
% Total	31 (32)	33 (31)	36 (37)	69 (68)
<b>Net Energy Deposition</b>				
Rate (GW)	1.45 (2.61)	7.70 (12.3)	6.02 (11.1)	
% Total	32 (33)	34 (31)	34 (36)	68 (67)
<b>Electron Precipitation</b>				
Rate (10 <sup>25</sup> s <sup>-1</sup> )	1.80 (3.51)	9.75 (15.2)	6.45 (14.3)	
% Total	34 (35)	36 (29)	30 (36)	66 (65)
<b>Outflowing Ions</b>				
Rate (10 <sup>24</sup> s <sup>-1</sup> )	0.78 (1.25)	3.88 (5.42)	2.05 (5.96)	
% Total	38 (33)	37 (28)	25 (39)	62 (67)

<sup>a</sup> Global (sum of Northern and Southern Hemisphere) quantities are italicized and shown in parentheses.

<sup>b</sup> October 1996 through November 1999, inclusive.

Hemisphere total for each budget (far right column in Table 1), even though storm phases comprise less than 31% of the study period.

Global rates shown in parentheses in Table 1 likewise indicate that storm phases are associated with 63–68% of the corresponding totals of global Alfvénic energy deposition, electron precipitation, and ion outflow budgets. However, both global rates and global budgets tend to accentuate storm recovery phase and to de-emphasize storm main phase relative to Northern Hemisphere counterparts. The Southern Hemisphere statistics are subject to greater uncertainty, since for each phase the number of Southern Hemisphere IAW observations is between 34% and 41% of the corresponding number of Northern Hemisphere observations (Table 1).

Given the variability of solar and geomagnetic activity in the course of an ~11-year solar cycle, the foregoing analysis would ideally be performed using Alfvén wave observations spanning an entire solar cycle. In lieu of such observations, the next best option is to determine the degree to which geomagnetic activity during the three-year study period is representative of geomagnetic activity during previous solar cycles.

Fig. 4 presents measures of geomagnetic activity over a 55-year period from 1957 to 2011, derived from the *Dst* index and calculated at 18-month intervals. This 55-year period covers the entirety of solar cycles 20–23 and most of solar cycle 19. The period surveyed for Alfvénic activity in this study, which is identical to the period surveyed by Hatch et al. (2016), is highlighted in green. Each box plot at far right indicates the upper and lower quartiles  $Q_3$  and  $Q_1$  and the median for each time series. The interquartile range  $IQR \equiv Q_3 - Q_1$  is used to define  $M_+ \equiv Q_3 + 1.5 IQR$  and  $M_- \equiv Q_1 - 1.5 IQR$ , which are respectively shown as the top and bottom lines of each box plot. Cross symbols at far right indicate the median for each measure of geomagnetic activity during the three-year FAST study period.

Fig. 4a shows how often geomagnetically quiescent periods (gray), storm main phase (red), and storm recovery phase (blue) occurred as a fraction of each 18-month interval, where each phase is identified based on the methodology of Chaston et al. (2015) that was summarized in Section 1. The two most apparent features are periods dominated almost entirely by quiescent conditions around 1965 and 2009 (within a year of the beginning of solar cycles 20 and 24); several local maxima are also evident in the time series, generally in correspondence with solar

maximum. Comparing the crosses and box plots at far right, it is evident that the relative occurrence frequency of geomagnetic quiescence and storm recovery phase over the three-year study period, 0.691 and 0.174, are slightly greater than the respective 55-year median values, .676 and 0.165. The occurrence frequency of main phase over the three-year period, 0.134, is slightly less than the corresponding 55-year median, 0.160. For each storm phase the occurrence frequency during the IAW study period is nonetheless well within the corresponding IQR.

Fig. 4b shows the median  $Dst_{min}$  for storms identified as either small (blue) or large (red), respectively corresponding to  $-50 < Dst_{min} \leq -20$  nT, or to  $Dst_{min} \leq -50$  nT. Statistics of large storms during the 55-year period indicate that 29 large-storm *Dst* minima are outliers, of which 22 lie below the lower bound of the y axis at  $-300$  nT. None of these occurred during the IAW study period. From the crosses and box plots at far right it is evident that the median  $Dst_{min}$  for small and large storms during the IAW study period are near corresponding 55-year median values.

The statistics in Fig. 4 uniformly indicate that geomagnetic conditions during the IAW study period are representative of periods of moderate, or perhaps slightly weak, geomagnetic activity during the past 55 years. It therefore seems likely that even during periods of moderate geomagnetic activity, the storm phase-associated contributions to IAW-related global energy deposition, particle precipitation, and ion outflow is dominant. In favor of this conclusion it should be pointed out that since no outlier storms occurred during the study period, an important class of storms not represented in our calculations are those with deep *Dst* minima; such storms would presumably correspond to the most dramatic enhancements in rates of energy deposition and outflow.

The rates of broadband electron energy deposition reported by Newell et al. (2009) provide some additional context for the calculated rates of electron energy deposition shown in Table 1. In their study the rate of broadband energy deposition during low solar wind driving, 0.6 GW (upper panel of their Fig. 4), is about 35% less than corresponding rate of IAW-related energy deposition in the Northern Hemisphere during geomagnetically quiescent periods (Fig. 2a), 0.91 GW. During high solar wind driving Newell et al. (2009) report that this rate increases to 4.8 GW, which is 6% less than the calculated rate in the Northern Hemisphere reported here for storm main phase, 5.08 GW. These differences between rates of broadband and IAW-related electron energy deposition seem reasonable given that the methodology for identification of broadband precipitation that they employ differs considerably from the methodology for IAW identification that we employ; differences could also be attributable to dissimilar methods for determination of quiescent periods employed in each study.

Lennartsson et al. (2004) have reported statistical hemispheric rates of O<sup>+</sup> and H<sup>+</sup> outflow using Polar satellite observations spanning a period overlapping most of the period considered in this study. The quiescent rate of IAW-related ion outflow in the Southern Hemisphere shown in Fig. 3,  $0.47 \times 10^{24} \text{ s}^{-1}$ , is ~15% of the  $2.8 \times 10^{24} \text{ s}^{-1}$  that they report as the average rate of ion outflow in the Southern Hemisphere during periods corresponding to IMF  $B_z > 3$  nT (*Dst* = -8 nT in their Table 1). During recovery phase the Southern Hemisphere rate of IAW-related ion outflow,  $3.91 \times 10^{24} \text{ s}^{-1}$ , is about 44% of their reported Southern Hemisphere average rate,  $\sim 9.0 \times 10^{24} \text{ s}^{-1}$ , during periods corresponding to IMF  $B_z > 3$  nT (*Dst* = -24 nT in their Table 1). These estimates imply that IAWs are associated with 15–45% of the ion outflow observed by Polar in the Southern Hemisphere, which is comparable to the Alfvén wave-associated proportion of net ion outflow, 15–34%, that has been reported by Chaston et al. (2007a). We only compare Southern Hemisphere rates of ion outflow reported in each study, since Polar perigee at  $\sim 2 R_E$  is nearest FAST apogee at 4180 km in the Southern Hemisphere, and Lennartsson et al. (2004) show that overall rates of outflow strongly depend on altitude.

As a final point on the cause of dayside storm enhancements, it is evident in Figs. 2 and 3 that during main and recovery phase in both

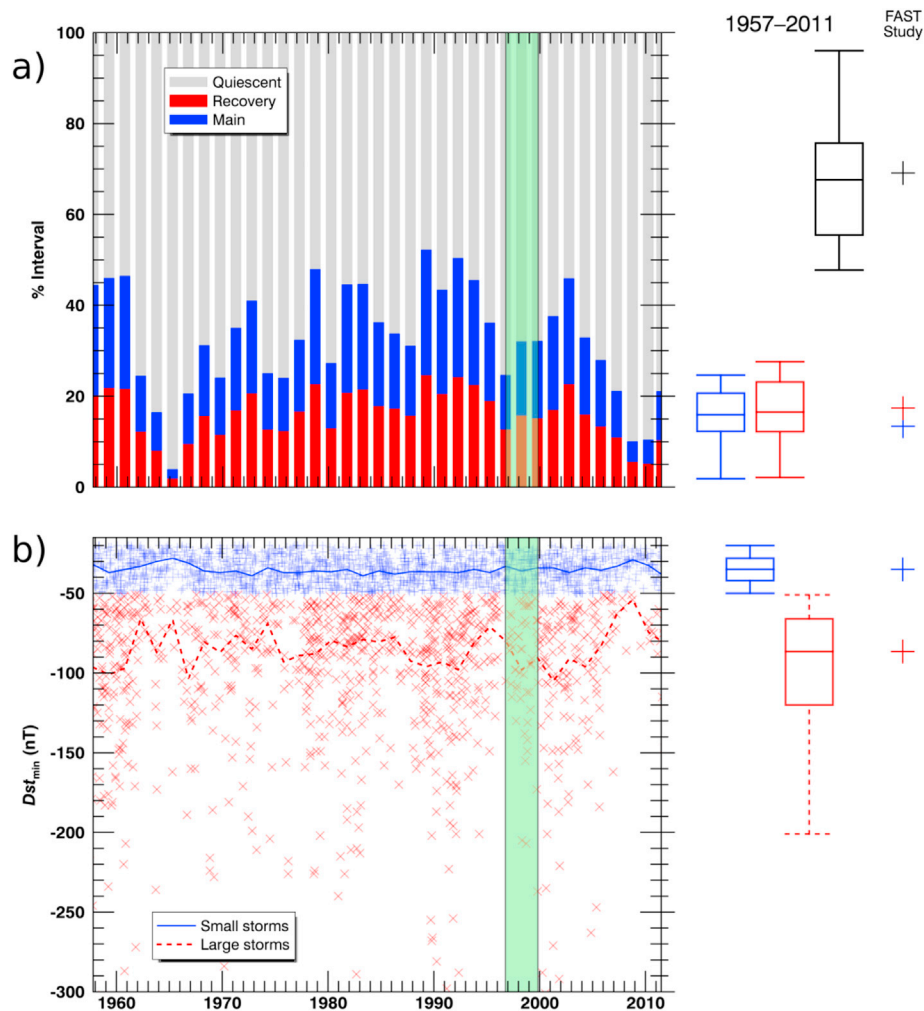


**Fig. 4.** Measures of geomagnetic activity derived from the  $Dst$  index for the 55-year period between 1957 and 2011, inclusive. (a) Occurrence frequency of geomagnetic quiescence (gray), storm main phase (red), and storm recovery phase (blue) as a fraction of each 18-month interval. (b) Median  $Dst_{\min}$  for small (solid blue line) and large (dashed red line) storms identified using the Anderson et al. (2015) methodology, with individual  $Dst_{\min}$  plotted as '+' or 'x' for small or large storms, respectively. Each time series is calculated over 18-month intervals. The three-year period covered by the FAST study (Oct 1996 through Nov 1999, inclusive) is highlighted in transparent green. The boxes at far right indicate, from top to bottom, the upper quartile Q3, median, and lower quartile Q1 for each time series. Horizontal lines above and below each box respectively indicate  $M_+$  and  $M_-$ , which are defined in the text. Cross symbols at far right indicate the median of each measure of geomagnetic activity during the three-year FAST study period. The vertical placement of box plots and cross symbols is relative to 0%. (For interpretation of the references to colour in this figure legend, the reader is referred to the web version of this article.)

hemispheres, rates of IAW-related energy deposition, electron precipitation, and ion outflow all show enhancements extending almost to 18 MLT. At these local times Alfvénic activity is unlikely to be associated with cusp processes. Another class of low-frequency waves, Pc5 oscillations, has been observed in the dusk sector in association with disturbed geomagnetic conditions (See Walker et al., 1982; Rae et al., 2005; Pili-penko et al., 2010, and references therein), though with the present data set we are unable to speculate on the relationship between Pc5 waves and small-scale Alfvén waves above the ionosphere.

## 6. Summary and conclusions

Geomagnetic storms dynamically influence magnetospheric and ionospheric processes on a variety of scales through coupling between the solar wind and the magnetosphere. The contribution of this study has been to estimate the high-latitude rates of energy deposition, electron precipitation, and ion outflow associated with inertial Alfvén waves for each geomagnetic storm phase, and to quantitatively partition the corresponding budgets by storm phase.

In particular, from a study of the storm phase-dependent, global-scale response of inertial Alfvén wave observations made by the FAST satellite between October 1996 and 1999, we conclude the following:

1. Global rates of IAW-related energy deposition, electron precipitation, and ion outflow increase by factors of 4–5 during storm main phase.
2. During the three-year period considered, storm main and recovery phases were associated with 63–68% of all IAW-related energy deposition, electron precipitation, and ion outflow. When the higher current density threshold ( $10 \mu\text{A}/\text{m}^2$ ) imposed by Hatch et al. (2016) is used in our analysis (Appendix A), the range becomes 68–78%.
3. Comparison of the three-year study period with 55 years of  $Dst$  measurements suggests that during periods of moderate geomagnetic activity ( $\sim 50$  storms per year, or an occurrence probability of  $\sim 0.16$  for both storm main and recovery phase), each geomagnetic storm phase is associated with  $\sim 30$ – $40\%$  of the total energy deposition, electron precipitation, and ion outflow that is associated with inertial Alfvén waves.

## Acknowledgments

S. M. Hatch thanks O. Verkhoglyadova at Caltech/Jet Propulsion Laboratory for feedback, suggestions, and several useful conversations during preparation of this manuscript. The authors gratefully acknowledge use of the  $Dst$  index, made available through the World Data Center for Geomagnetism, Kyoto (Kyoto World Data Center, <http://wdc.kugi>).

kyoto-u.ac.jp/), and the Hermanus, Honolulu, Kakioka, San Juan, and INTERMAGNET observatories. Work at Space Sciences Laboratory was supported by NASA grants NNX16AG69G and NNX15AF57G; work at

Dartmouth was supported by NASA grant NNX12AI44G, sub-award W000726838 to grant NNX15AL08G, and NASA Earth and Space Science Fellowship Program–Grant NNX14AO03H.

#### Appendix A. Time-averaged gross rates using a $10\text{-}\mu\text{A}/\text{m}^2$ current density threshold

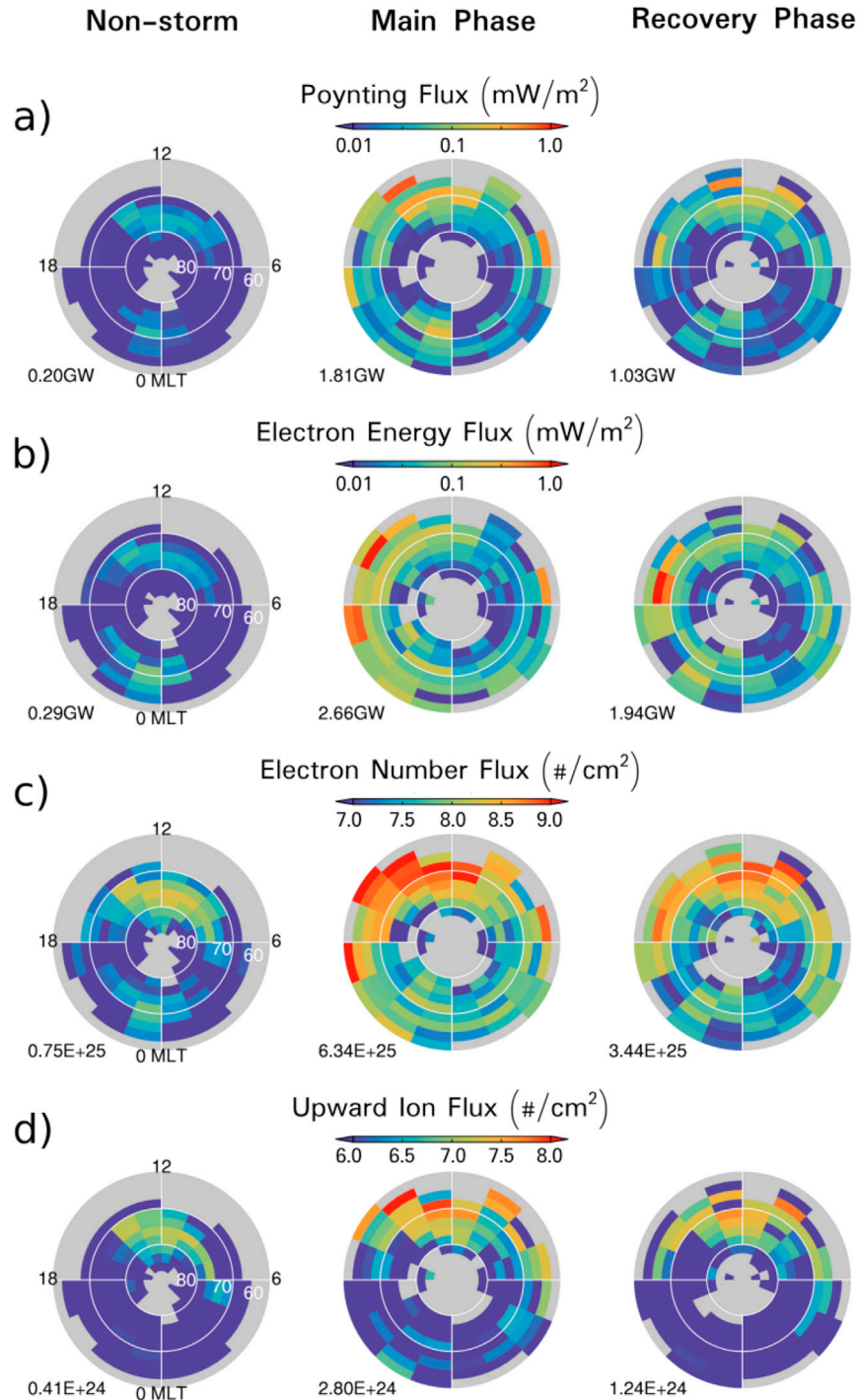


**Fig. A1.** Average fluxes associated with  $\geq 10\text{-}\mu\text{A}/\text{m}^2$  IAWs in the Northern Hemisphere during geomagnetically quiescent periods (left panels), storm main phase (center panels), and storm recovery phase (right panels). (a) Poynting flux. (b) Loss-cone electron energy flux. (c) Loss-cone electron number flux. (d) Upward ion flux.

Here we provide a condensed version of the analysis found in Section 4 using the original  $10\text{-}\mu\text{A}/\text{m}^2$  current density threshold imposed by Hatch et al. (2016). Our intention is to indicate whether (and if so, how) a more stringent threshold modifies the average fluxes presented in Section 4 as well as corresponding rates of energy deposition, precipitation, and ion outflow.

As discussed in Section 3, increasing the current density threshold tends to decrease the number of IAW observations within a given MLT-ILAT bin, which in turn decreases the calculated frequency of IAW observation. Since the average flux  $\langle Q \rangle$  in (2) depends on the frequency of IAW observation, increasing the current density threshold causes the calculated average fluxes and global rates corresponding to each flux quantity to decrease. Therefore,

the primary expected effect of increasing the current density threshold is a decrease in all average flux quantities and hemispheric/global rates presented in Section 4.

Fig. A1 shows each flux quantity that is shown in Fig. 2 for the Northern Hemisphere. Although the average intensities of each flux quantity in Fig. A1 are diminished relative to corresponding intensities in Fig. 2, the overall statistical pattern associated with each quantity for each storm phase is largely the same. For instance, both figures show that during quiescent periods (left panels) the most prominent statistical features are located in the cusp region and premidnight. Both figures also indicate that during storm main phase (center panels) the greatest flux intensities and overall rates of energy deposition, precipitation, and outflow are observed, and that flux intensities and associated hemispheric rates tend to decrease during storm recovery phase (right panels).

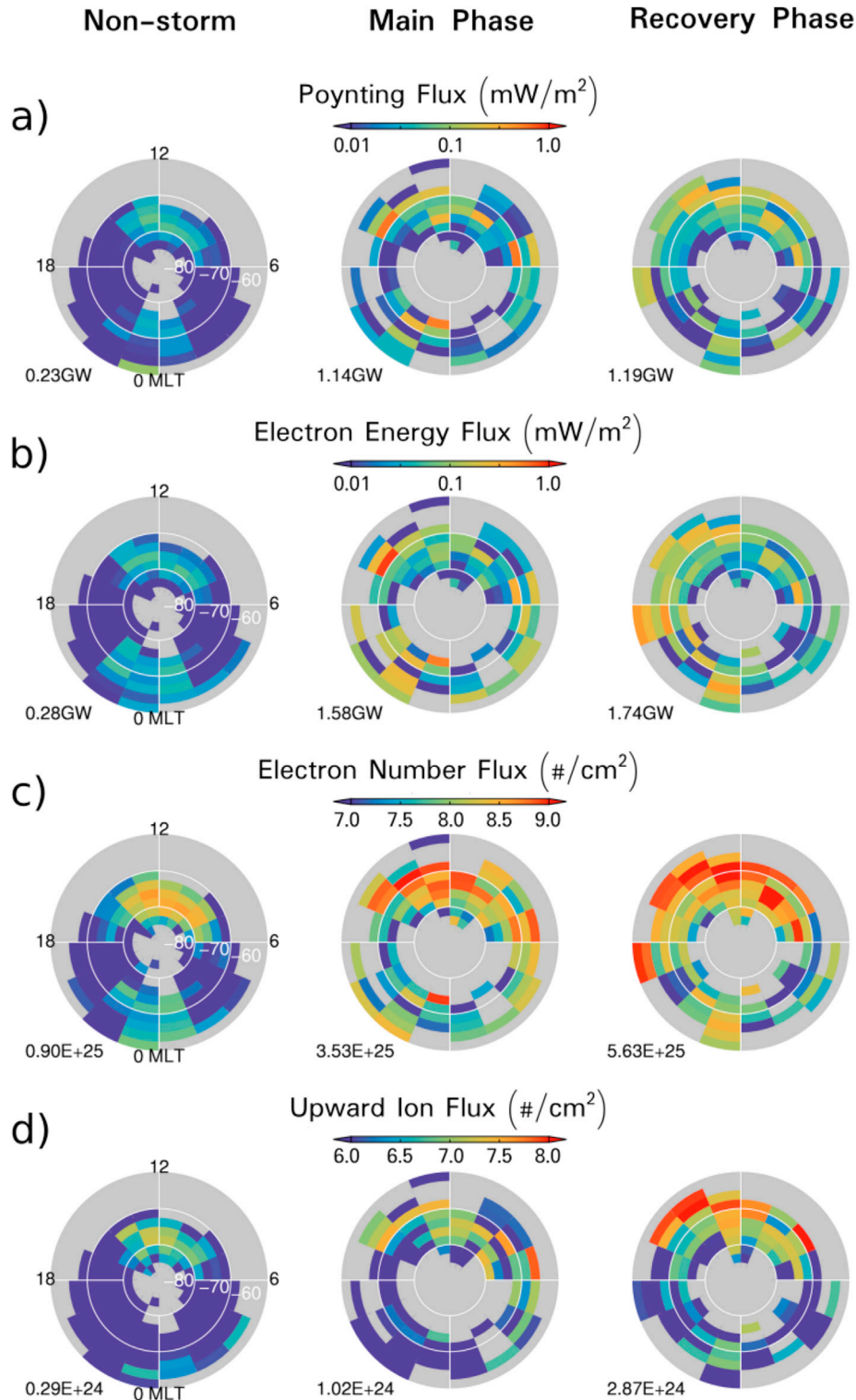


Fig. A2. Average fluxes associated with  $\geq 10\text{-}\mu\text{A}/\text{m}^2$  IAWs in the Southern Hemisphere during geomagnetically quiescent periods (left panels), storm main phase (center panels), and storm recovery phase (right panels). (a) Poynting flux. (b) Loss-cone electron energy flux. (c) Loss-cone electron number flux. (d) Upward ion flux.

Figure A2 shows the same quantities presented in Fig. 3 for the Southern Hemisphere. As with Figs. A1 and 2 the overall intensities of each average

flux quantity in Fig. A2 are diminished relative to corresponding intensities in Fig. 3, but the overall statistical patterns are the same in each figure.

Comparison of Table 1 and A1 shows that imposing a  $10\text{-}\mu\text{A}/\text{m}^2$  current density threshold reduces the number of IAW observations by more than 50% for each storm phase, which consequently reduces the hemispheric and global rates corresponding to each flux quantity, as anticipated. A less obvious ramification of increasing the current density threshold is that storm main and recovery phase-associated contributions to IAW-related global energy deposition, particle precipitation, and ion outflow are even more pronounced (68–78%) relative to the contributions shown in Table 1 (far right column in each table).

**Table A1**  
Storm Phase–Partitioned Rates and Budgets Using  $10\text{-}\mu\text{A}/\text{m}^2$  Current Density Threshold<sup>a</sup>

	Quiescence	Main Phase	Recovery Phase	M+R Combined
<b>IAW Observations</b>				
N	79,690 (110,301)	20,495 (28,411)	25,835 (39,639)	46,330 (68,050)
<b>Wave Energy Deposition</b>				
Rate (GW)	0.20 (0.43)	1.81 (2.95)	1.03 (2.22)	
% Total	25 (28)	43 (37)	32 (36)	75 (72)
<b>Electron Energy Deposition</b>				
Rate (GW)	0.29 (0.57)	2.66 (4.24)	1.94 (3.68)	
% Total	22 (25)	40 (40)	38 (40)	78 (75)
<b>Net Energy Deposition</b>				
Rate (GW)	0.49 (1.00)	4.47 (7.19)	2.97 (5.90)	
% Total	23 (26)	41 (36)	36 (38)	77 (74)
<b>Electron Precipitation</b>				
Rate ( $10^{25}\text{ s}^{-1}$ )	0.75 (1.65)	6.34 (9.87)	3.44 (9.07)	
% Total	26 (28)	43 (33)	31 (39)	74 (72)
<b>Outflowing Ions</b>				
Rate ( $10^{24}\text{ s}^{-1}$ )	0.41 (0.70)	2.80 (3.82)	1.24 (4.11)	
% Total	32 (28)	43 (30)	25 (42)	68 (72)

<sup>a</sup> Global (sum of Northern and Southern Hemisphere) quantities are italicized and shown in parentheses.

## References

- Aikio, A.T., Blomberg, L.G., Marklund, G.T., Yamauchi, M., 1996. On the origin of the high-altitude electric field fluctuations in the auroral zone. *J. Geophys. Res. Space Phys.* 101 (A12), 27157–27170.
- Anderson, B.R., Millan, R.M., Reeves, G.D., Friedel, R.H.W., 2015. Acceleration and loss of relativistic electrons during small geomagnetic storms. *Geophys. Res. Lett.* 42, 10113–10119.
- Andersson, L., Ivchenko, N., Clemmons, J., Namgaladze, A.A., Gustavsson, B., Wahlund, J.E., Eliasson, L., Yurik, R.Y., 2002. Electron signatures and Alfvén waves. *J. Geophys. Res. Sp. Phys.* 107 (A9), 1244.
- Bogdanova, Y.V., Fazakerley, A.N., Owen, C.J., Klecker, B., Cornilleau-Wehrin, N., Grison, B., André, M., Cargill, P., Rème, H., Bosqued, J.M., Kistler, L.M., Balogh, A., 2004. Correlation between suprathermal electron bursts, broadband extremely low frequency waves, and local ion heating in the midaltitude cleft/low-latitude boundary layer observed by Cluster. *J. Geophys. Res. Space Phys.* 109 (A12), 1–7.
- Brito, T., Woodger, L., Hudson, M., Millan, R., 2012. Energetic radiation belt electron precipitation showing ULF modulation. *Geophys. Res. Lett.* 39 (22), 1–7.
- Cane, H.V., Richardson, I.G., 2003. Interplanetary coronal mass ejections in the near-Earth solar wind during 19962002. *J. Geophys. Res.* 108 (A4), 1156.
- Carlson, C.W., McFadden, J.P., Turin, P., Curtis, D.W., Magoncelli, A., 2001. The electron and ion plasma experiment for FAST. *Space Sci. Rev.* 98 (1), 33–66.
- Cattell, C., Dombeck, J., Carlson, C., McFadden, J., 2006. FAST observations of the solar illumination dependence of downgoing auroral electron beams: relationship to electron energy flux. *J. Geophys. Res.* 111, A02201.
- Chaston, C.C., Bonnell, J.W., Carlson, C.W., Berthomier, M., Peticolas, L.M., Roth, I., McFadden, J.P., Ergun, R.E., Strangeway, R.J., Nov 2002. Electron acceleration in the ionospheric Alfvén resonator. *J. Geophys. Res. Sp. Phys.* 107 (A11), SMP 41–SMP 41–16.
- Chaston, C.C., Bonnell, J.W., Carlson, C.W., McFadden, J.P., Ergun, R.E., Strangeway, R.J., 2003a. Properties of small-scale Alfvén waves and accelerated electrons from FAST. *J. Geophys. Res. Space Phys.* 108 (A4), 1–16.
- Chaston, C.C., Bonnell, J.W., Kletzing, C.A., Hospodarsky, G.B., Wygant, J.R., Smith, C., 2015. Broadband low-frequency electromagnetic waves in the inner magnetosphere. *J. Geophys. Res. Space Phys.* 120, 8603–8615.
- Chaston, C.C., Bonnell, J.W., Reeves, G.D., Skoug, R.M., May 2016. Driving ionospheric outflows and magnetospheric O+ energy density with Alfvén waves. *Geophys. Res. Lett.* 43 (10), 4825–4833.
- Chaston, C.C., Carlson, C.W., McFadden, J.P., Ergun, R.E., Strangeway, R.J., 2007a. How important are dispersive Alfvén waves for auroral particle acceleration? *Geophys. Res. Lett.* 34, L07101.
- Chaston, C.C., Genot, V., Bonnell, J.W., Carlson, C.W., McFadden, J.P., Ergun, R.E., Strangeway, R.J., Lund, E.J., Hwang, K.J., 2006. Ionospheric erosion by Alfvén waves. *J. Geophys. Res. Space Phys.* 111, A03206.
- Chaston, C.C., Peticolas, L.M., Bonnell, J.W., Carlson, C.W., Ergun, R.E., McFadden, J.P., Strangeway, R.J., Feb 2003b. Width and brightness of auroral arcs driven by inertial Alfvén waves. *J. Geophys. Res. Space Phys.* 108 (A2), 1091.
- Chaston, C.C., Wilber, M., Mozer, F.S., Fujimoto, M., Goldstein, M.L., Acuna, M., Rème, H., Fazakerley, A., Oct 2007b. Mode conversion and anomalous transport in kelvin-helmholtz vortices and kinetic Alfvén waves at the Earth's magnetopause. *Phys. Rev. Lett.* 99 (17), 175004.
- Chen, L.J., Kletzing, C.A., Hu, S., Bounds, S.R., 2005. Auroral electron dispersion below inverted-V energies: resonant deceleration and acceleration by Alfvén waves. *J. Geophys. Res. Sp. Phys.* 110 (A10), 1–16.
- Cosgrove, R.B., Jan 2016. Does a localized plasma disturbance in the ionosphere evolve to electrostatic equilibrium? Evidence to the contrary. *J. Geophys. Res. Sp. Phys.* 121 (1), 649–687.
- Delcourt, D.C., Mar 2002. Particle acceleration by inductive electric fields in the inner magnetosphere. *J. Atmos. Solar-Terrestrial Phys.* 64 (56), 551–559.
- Dunlop, M.W., Zhang, Q., Xiao, C., He, J., Pu, Z., Fear, R., Shen, C., Escoubert, C.P., 2009. Reconnection at high latitudes: antiparallel merging. *Phys. Rev. Lett.* 102 (075005), 1–4.
- Gao, X., Li, W., Bortnik, J., Thorne, R.M., Lu, Q., Ma, Q., Tao, X., Wang, S., Jun 2015. The effect of different solar wind parameters upon significant relativistic electron flux dropouts in the magnetosphere. *Journal of Geophysical Research: Space Phys.* 120 (6), 4324–4337.
- Genot, V., Louarn, P., Mottez, F., 2004. Alfvén wave interaction with inhomogeneous plasmas: acceleration and energy cascade towards small-scales. *Ann. Geophys.* 22 (6), 2081–2096.
- Gonzalez, W.D., Joselyn, J.A., Kamide, Y., Kroehl, H.W., Rostoker, G., Tsurutani, B.T., Vasyliunas, V.M., 1994. What is a geomagnetic storm? *J. Geophys. Res.* 99 (A4), 5771.
- Grzesiak, M., 2000. Ionospheric Alfvén resonator as seen by Freja satellite. *Geophys. Res. Lett.* 27 (7), 923–926.
- Guo, J., Feng, X., Emery, B.A., Zhang, J., Xiang, C., Shen, F., Song, W., May 2011. Energy transfer during intense geomagnetic storms driven by interplanetary coronal mass ejections and their sheath regions. *J. Geophys. Res. Space Phys.* 116 (A5).
- Hamilton, D.C., Gloeckler, G., Ipavich, F.M., Stüdemann, W., Wilken, B., Kremser, G., 1988. Ring current development during the great geomagnetic storm of February 1986. *J. Geophys. Res.* 93 (A12), 14343.
- Hasegawa, A., Oct 1976. Particle acceleration by MHD surface wave and formation of aurora. *J. Geophys. Res.* 81 (28), 5083–5090.
- Hatch, S.M., Chaston, C.C., Labelle, J., 2016. Alfvén wavelike driven ionospheric mass outflow and electron precipitation during storms. *J. Geophys. Res. Space Phys.* 121.
- Hirano, Y., Fukunishi, H., Kataoka, R., Hasunuma, T., Nagatsuma, T., Miyake, W., Matsuoka, A., 2005. Evidence for the resonator of inertial Alfvén waves in the cusp topside ionosphere. *J. Geophys. Res. Sp. Phys.* 110 (A7).
- Hoshino, M., Mukai, T., Terasawa, T., Shinohara, I., Nov 2001. Suprathermal electron acceleration in magnetic reconnection. *J. Geophys. Res. Sp. Phys.* 106 (A11), 25979–25997.
- Hudson, M., Brito, T., Elkington, S., Kress, B., Li, Z., Wiltberger, M., 2012. Radiation belt 2D and 3D simulations for CIR-driven storms during Carrington Rotation 2068. *J. Atmos. Solar Terr. Phys.* 83, 51–62.
- Kamide, Y., Baumjohann, W., Daglis, I.A., Gonzalez, W.D., Grande, M., Joselyn, J.A., McPherron, R.L., Phillips, J.L., Reeves, E.G.D., Rostoker, G., Sharma, A.S., Singer, H.J., Tsurutani, B.T., Vasyliunas, V.M., 1998. Current understanding of magnetic storms: storm-substorm relationships. *J. Geophys. Res.* 103 (A8), 17705.
- Keiling, A., 2009. Alfvén waves and their roles in the dynamics of the Earth's magnetotail: a review. *Space Sci. Rev.* 142, 73–156.

- Keiling, A., Wygant, J.R., Cattell, C., Peria, W., Parks, G., Temerin, M., Mozer, F.S., Russell, C.T., Kletzing, C.A., 2002. Correlation of Alfvén wave Poynting flux in the plasma sheet at 47 RE with ionospheric electron energy flux. *J. Geophys. Res.* 107 (A7), 1132.
- Keiling, A., Wygant, J.R., Cattell, C., Temerin, M., Mozer, F.S., Kletzing, C.A., Scudder, J.D., Russell, C.T., Lotko, W., Streltsov, A.V., 2000. Large Alfvén wave power in the plasma sheet boundary layer during the expansion phase of substorms. *Geophys. Res. Lett.* 27 (19), 3169–3172.
- Keiling, A., Wygant, J.R., Cattell, C.A., Mozer, F.S., Russell, C.T., Jan 2003. The global morphology of wave poynting flux: powering the aurora. *Science* 299, 383.
- Kelley, M.C., 1989. *The Earth's Ionosphere: Plasma Physics and Electrodynamics*. Academic, San Diego, California.
- Khazanov, G.V., Glocer, A., Sibeck, D.G., Tripathi, A.K., Detweiler, L.G., Avanan, L.A., Singhal, R.P., Jul 2016. Ionosphere-magnetosphere energy interplay in the regions of diffuse aurora. *J. Geophys. Res. Space Phys.* 121 (7), 1–26.
- Kletzing, C.A., 1994. Electron acceleration by kinetic Alfvén waves. *J. Geophys. Res.* 99 (A6), 11095–11103.
- Kletzing, C.A., Hu, S., 2001. Alfvén wave generated electron time dispersion. *Geophys. Res. Lett.* 28 (4), 693–696.
- Knudsen, D.J., 1996. Spatial modulation of electron energy and density by nonlinear stationary inertial Alfvén waves. *J. Geophys. Res.* 101 (A5), 10761.
- Kronberg, E.A., Iannis, M.A.-A., Delcourt, D.C., Grigorenko, E.E., Kistler, L.M., Kuzichev, I.V., Liao, J., Maggiolo, R., Malova, H.V., Orlova, K.G., Peroomian, V., Shklyar, D.R., Shprits, Y.Y., Welling, D.T., Zelenyi, L.M., 2014. Circulation of heavy ions and their dynamical effects in the magnetosphere: recent observations and models. *Space Sci. Rev.* 184, 173–235.
- Lee, A.R., Newell, P.T., Gjerloev, J., Liou, K., 2010. Relatively low-latitude wave aurora and substorms. *Geophys. Res. Lett.* 37 (6), 1–4.
- Lennartsson, O.W., Collin, H.L., Peterson, W.K., 2004. Solar wind control of Earth's H<sup>+</sup> and O<sup>+</sup> outflow rates in the 15-eV to 33-keV energy range. *J. Geophys. Res. Sp. Phys.* 109 (A12), 1–14.
- Liemohn, M.W., Kozyra, J.U., 2002. Assessing the importance of convective and inductive electric fields in forming the stormtime ring current. In: *Sixth Int. Conf. Substorms*. Univ. of Washington, Seattle, p. 456.
- Lotko, W., Oct 2004. Inductive magnetosphere-ionosphere coupling. *J. Atmos. Solar Terr. Phys.* 66, 1443–1456.
- Lotko, W., 2007. The magnetosphere ionosphere system from the perspective of plasma circulation: a tutorial. *J. Atmos. Solar Terr. Phys.* 69, 191–211.
- Lotko, W., Smith, R.H., Zhang, B., Ouellette, J.E., Brambles, O.J., Lyon, J.G., 2014. Ionospheric control of magnetotail reconnection. *Science* 345, 184.
- Lysak, R., Song, Y., Jan 2006. Magnetosphere-ionosphere coupling by Alfvén waves: beyond current continuity. *Adv. Sp. Res.* 38 (8), 1713–1719.
- Lysak, R.L., 1993. Generalized model of the ionospheric Alfvén resonator. In: *Auror. Plasma Dyn. American Geophysical Union*, pp. 121–128.
- Lysak, R.L., Jul 2004. Magnetosphere-ionosphere coupling by Alfvén waves at midlatitudes. *J. Geophys. Res. Sp. Phys.* 109 (A7).
- Lysak, R.L., Song, Y., 2000. Propagation of Alfvén waves at the plasma sheet boundary layer. In: *Pulkkinen, T., Ganushkina, N. (Eds.), Proc. 7th Inter-Natl. Conf. Substorms*. Finnish Meteorological Institute, Helsinki, pp. 1–6.
- Lysak, R.L., Song, Y., 2003. Kinetic theory of the Alfvén wave acceleration of auroral electrons. *J. Geophys. Res.* 108 (A4), 8005.
- Lysak, R.L., Song, Y., Sciffer, M.D., Waters, C.L., Jan 2015. Propagation of Pi2 pulsations in a dipole model of the magnetosphere. *J. Geophys. Res. Sp. Phys.* 120 (1), 355–367.
- Mareschal, M., Aug 1976. On the problem of simulating the Earth's induction effects in modeling polar magnetic substorms. *Rev. Geophys.* 14 (3), 403–409.
- Mishin, V.V., Mishin, V.M., Lunyushkin, S.B., Pu, Z., Wang, C., 2015. Strong induction effects during the substorm on 27 August 2001. *Earth, Planets Sp.* 67 (1), 162.
- Newell, P.T., Lee, A.R., Liou, K., Ohtani, S.-I., Sotirelis, T., Wing, S., Sep 2010. Substorm cycle dependence of various types of aurora. *J. Geophys. Res. Space Phys.* 115 (A9).
- Newell, P.T., Sotirelis, T., Liou, K., Meng, C.-I., Rich, F.J., Jan 2007. A nearly universal solar wind-magnetosphere coupling function inferred from 10 magnetospheric state variables. *J. Geophys. Res. Sp. Phys.* 112 (A1).
- Newell, P.T., Sotirelis, T., Wing, S., 2009. Diffuse, monoenergetic, and broadband aurora: the global precipitation budget. *J. Geophys. Res.* 114, A09207.
- Ohtani, S., Korth, H., Keika, K., Zheng, Y., Brandt, P.C., Mende, S.B., May 2010. Inductive electric fields in the inner magnetosphere during geomagnetically active periods. *J. Geophys. Res. Sp. Phys.* 115 (A5).
- Pilipenko, V., Kozyreva, O., Belakhovsky, V., Engebretson, M.J., Samsonov, S., 2010. Generation of magnetic and particle pc5 pulsations during the recovery phase of strong magnetic storms. *Proceedings of the Royal Society of London A: Mathematical. Phys. Eng. Sci.* 466 (2123), 3363–3390.
- Poliakov, S.V., Rapoport, V.O., Oct 1981. The ionospheric Alfvén resonator. *Geomagn. Aeron.* 21, 816–822.
- Rae, I.J., Donovan, E.F., Mann, I.R., Fenrich, F.R., Watt, C.E.J., Milling, D.K., Lester, M., Lavraud, B., Wild, J.A., Singer, H.J., Rème, H., Balogh, A., Dec 2005. Evolution and characteristics of global Pc5 ULF waves during a high solar wind speed interval. *J. Geophys. Res. Space Phys.* 110 (A12).
- Rankin, R., Samson, J.C., Tikhonchuk, V.T., 1999. Parallel electric fields in dispersive shear Alfvén waves in the dipolar magnetosphere. *Geophys. Res. Lett.* 26 (24), 3601–3604.
- Rother, M., Schlegel, K., Lühr, H., 2007. CHAMP observation of intense kilometer-scale field-aligned currents, evidence for an ionospheric Alfvén resonator. *Ann. Geophys.* 25 (7), 1603–1615.
- Shepherd, S.G., Sep 2014. Altitude-adjusted corrected geomagnetic coordinates: definition and functional approximations. *J. Geophys. Res. Sp. Phys.* 119 (9), 7501–7521.
- Song, P., Vasyliunas, V.M., 2014. Inductive-dynamic coupling of the ionosphere with the thermosphere and the magnetosphere. In: *Model. Ionos. Syst.* John Wiley & Sons, Ltd, pp. 201–215. Ch. 17.
- Song, Y., Lysak, R.L., 2006. Displacement current and the generation of parallel electric fields. *Phys. Rev. Lett.* 96 (14), 1–4.
- Stasiewicz, K., Bellan, P., Chaston, C., Kletzing, C., Lysak, R., Maggs, J., Pokhotelov, O., Seyler, C., Shukla, P., Stenflo, L., Streltsov, A., Wahlund, J.-E., 2000. Small scale alfvénic structure in the aurora. *Space Sci. Rev.* 92, 423–533.
- Stasiewicz, K., Holmgren, G., Zanetti, L., 1998. Density depletions and current singularities observed by Freja. *J. Geophys. Res.* 103 (A3), 4251–4260.
- Strangeway, R.J., Ergun, R.E., Su, Y., Carlson, C.W., Elphic, R.C., 2005. Factors controlling ionospheric outflows as observed at intermediate altitudes. *J. Geophys. Res. Space Phys.* 110, A03221.
- Takada, T., Nakamura, R., Baumjohann, W., Seki, K., Vörös, Z., Asano, Y., Volwerk, M., Runov, A., Zhang, T.L., Balogh, A., Paschmann, G., Torbert, R.B., Klecker, B., Rème, H., Puhl-Quinn, P.A., Canu, P., Décreau, P.M.E., 2006. Alfvén waves in the near-PSBL lobe: cluster observations. *Ann. Geophys.* 224 (1997), 1001–1013.
- Tanaka, H., Saito, Y., Asamura, K., Ishii, S., Mukai, T., 2005a. High time resolution measurement of multiple electron precipitations with energy-time dispersion in high-latitude part of the cusp region. *J. Geophys. Res. Space Phys.* 110 (A7), 1–10.
- Tanaka, H., Saito, Y., Asamura, K., Mukai, T., 2005b. Numerical modeling of electron energy-time dispersions in the high-latitude part of the cusp region. *J. Geophys. Res.* 110 (A05213), 1–16.
- Thayer, J.P., Semeter, J., Jul 2004. The convergence of magnetospheric energy flux in the polar atmosphere. *J. Atmos. Solar Terr. Phys.* 66 (10), 807–824.
- Tsurutani, B.T., Gonzalez, W.D., Gonzalez, A.L.C., Guarnieri, F.L., Gopalswamy, N., Grande, M., Kamide, Y., Kasahara, Y., Lu, G., Mann, I., McPherron, R., Soraas, F., Vasyliunas, V., 2006a. Corotating solar wind streams and recurrent geomagnetic activity: a review. *J. Geophys. Res.* 111, A07S01.
- Tsurutani, B.T., McPherron, R.L., Gonzalez, W.D., Lu, G., Gopalswamy, N., Guarnieri, F.L., 2006b. Magnetic storms caused by corotating solar wind streams. In: *Recurrent Magnetic Storms: Corotating Solar Wind Streams*. American Geophysical Union, pp. 1–17.
- Walker, A.D.M., Greenwald, R.A., Korth, A., Kremser, G., Nov 1982. STARE and GEOS 2 observations of a storm time Pc 5 ULF pulsation. *J. Geophys. Res. Space Phys.* 87 (A11), 9135–9146.
- Watt, C.E.J., Rankin, R., Jan 2009. Electron trapping in shear Alfvén waves that power the aurora. *Phys. Rev. Lett.* 102 (4), 45002.
- Watt, C.E.J., Rankin, R., 2012. Alfvén wave acceleration of auroral electrons in warm magnetospheric plasma. In: *Keiling, A., Donovan, E., Bagenal, F., Karlsson, T. (Eds.), Auroral Phenomenology and Magnetospheric Processes: Earth and Other Planets*, vol. 197. American Geophysical Union, Washington, D.C, pp. 251–260.
- Watt, C.E.J., Rankin, R., Rae, I.J., Wright, D., 2005. Self-consistent electron acceleration due to inertial Alfvén wave pulses. *J. Geophys. Res.* 110, A10S07.
- Welling, D.T., Jordanova, V.K., Glocer, A., Toth, G., Liemohn, M.W., Weimer, D.R., Jun 2015. The two-way relationship between ionospheric outflow and the ring current. *J. Geophys. Res. Space Phys.* 120 (6), 4338–4353.
- Wu, D.J., Feng, H.Q., Li, B., He, J.S., 2016. Nature of turbulence, dissipation, and heating in Space plasmas: from Alfvén waves to kinetic Alfvén waves. *J. Geophys. Res. Space Phys.* 121 (8), 7349–7352.
- Yoshikawa, A., Itonaga, M., Jan 1996. Reflection of shear Alfvén waves at the ionosphere and the divergent Hall current. *Geophys. Res. Lett.* 23 (1), 101–104. <https://doi.org/10.1029/95GL03580>.
- Zhang, B., Lotko, W., Brambles, O., Xi, S., Wiltberger, M., Lyon, J., 2014. Solar wind control of auroral Alfvénic power generated in the magnetotail. *J. Geophys. Res. Space Phys.* 119 (3), 1734–1748.